Giant proximity exchange and valley splitting in TMDC/hBN/(Co, Ni) heterostructures

Klaus Zollner,[1,*] Paulo E. Faria Junior,[1] and Jaroslav Fabian[1]

[1] *Institute for Theoretical Physics, University of Regensburg, 93040 Regensburg, Germany*

(Dated: October 30, 2019)

We investigate the proximity-induced exchange coupling in transition-metal dichalcogenides (TMDCs), originating from spin injector geometries composed of hexagonal boron-nitride (hBN) and ferromagnetic (FM) cobalt (Co) or nickel (Ni), from first-principles. We employ a minimal tight-binding Hamiltonian that captures the low energy bands of the TMDCs around K and K' valleys, to extract orbital, spin-orbit, and exchange parameters. The TMDC/hBN/FM heterostructure calculations show that due to the hBN buffer layer, the band structure of the TMDC is preserved, with an additional proximity-induced exchange splitting in the bands. We extract proximity exchange parameters in the 1–10 meV range, depending on the FM. The combination of proximity-induced exchange and intrinsic spin-orbit coupling (SOC) of the TMDCs, leads to a valley polarization, translating into magnetic exchange fields of tens of Tesla. The extracted parameters are useful for subsequent exciton calculations of TMDCs in the presence of a hBN/FM spin injector. Our calculated absorption spectra show a large splitting of the first exciton peak; in the case of MoS_2/hBN/Co we find a value of about 8 meV, corresponding to about 50 Tesla external magnetic field in bare TMDCs. The reason lies in the band structure, where a hybridization with Co d orbitals causes a giant valence band exchange splitting of more than 10 meV. Structures with Ni do not show any d level hybridization features, but still sizeable proximity exchange and exciton peak splittings of around 2 meV are present in the TMDCs.

Keywords: TMDC, heterostructures, proximity exchange

I. INTRODUCTION

Spintronics is based on the efficient injection, transport, manipulation and detection of spins in a material[1–3]. The current generation of spintronics devices employ hybrid geometries consisting of several two-dimensional (2D) materials[4,5] in order to overcome intrinsic limitations of the transport medium. A new branch of physics has emerged, which is solely dedicated to the interface engineering[6,7] of those ultrathin layers, including semiconductors, ferromagnets and superconductors, leading to new device technologies.

The most prominent example in this field is graphene, which has intrinsically outstanding spin and charge transport properties. Since several years now, physicists study graphene based spintronics devices[2] and have found an efficient way to inject spins via FM/insulator tunnel junctions into graphene[8–13]. Nonlocal measurement geometries reveal the spin transport properties of graphene, which can be modified by the presence of various 2D materials in van der Waals heterostructues. Currently, state of the art spin transport geometries are based on hBN encapsulated graphene[10,12,14,15], where spins are injected by FMs, with giant mobilities up to 10^6 cm^2/Vs[16–18] and spin lifetimes exceeding 10 ns[10]. The insulating hBN is ideal to reduce the contact resistance to the FM and helps to preserve the linear dispersion of graphene, which is desired for spin transport[19]. Also oxide insulators are used, such as MgO and SiO_2, resulting in less efficient spin injection[14]. The manipulation of spins can be achieved by inducing SOC or exchange coupling from proximity. For example, a TMDC in proximity to graphene, induces strong valley Zeeman spin-orbit fields on the order of 1 meV[20–22], significantly reducing spin lifetimes in graphene to about 10 ps[23–25], but leading to giant spin relaxation anisotropies (the ratio of out-of-plane to in-plane spin lifetime) of about 10[22–27]. Additionally, it has been demonstrated that a TMDC can be utilized for optical spin injection in graphene[21,25,28], relevant for the field of optospintronics.

Recently, there has been a lot of effort to use also other 2D materials such as phosphorene or TMDCs as the transport medium. The advantage is that they are already semiconducting, making them suitable for electronic and spintronic devices[1,3] such as spin diodes and field effect transistors[29–32]. In the case of phosphorene, very little is known about its spin transport properties[33–35]; the electronic ones are highly anisotropic and show large mobilities[36,37]. Furthremore, measurements combined with first-principles calculations show, that hBN is also an ideal tunnel barrier, when injecting spin polarized carriers from Co into phosphorene[35].

Monolayer TMDCs have a band gap in the optical range and the valley degree of freedom plays a major role[38–43] in their (opto-) electronic properties. The helicity selective excitation of carriers with certain spin in a certain valley at the same excitation energy, makes those materials very attractive for the field of valleytronics[44–48]. By an exchange field one can break the time-reversal symmetry of the TMDC, the degeneracy of the valleys, and introduce valley polarization. In an external magnetic field, the valley splitting rises roughly linear with 0.1 – 0.2 meV/T[49–52], such that large fields are required to get a sizable effect. A much better perspective to achieve large valley polarization in

TMDCs is by the proximity exchange effect. Indeed, placing the TMDC on a magnetic substrate, giant valley splittings can be achieved, ranging from few to hundreds of meV[47,48,53–60], which can additionally be tuned by gating and twisting[61].

For spin injection, one can either contact the TMDC with metal or metal/insulator interfaces or inject them optically[62,63]. In the former case, studying the dependence of the Schottky barrier on the used electrode is crucial[64–71]. It turns out that a hBN tunnel barrier is also a good choice here, preserving the intrinsic properties of the TMDC while enormously reducing the contact resistance[65,72–74]. Also other insulating barriers, such as TiO_2, MgO or Al_2O_3[75–79] are promising candidates, where the thickness of the barrier plays an important role for the efficiency of spin injection. The contact resistance can also be decreased by strong electron doping[80] or using graphene electrodes[81].

Electronic and spin transport[82–85] in TMDCs is becoming an important topic. It has been shown that the carrier mobility increases with the number of TMDC layers[69,84], due to reduced Coulomb scattering in thicker samples[86], while phonon scattering limits the room temperature mobility[85]. Spin transport has been studied on a theoretical level[87–90], while spin injection has been demonstrated electrically[47,76] and optically[63], showing spin diffusion lengths of about 200 nm in multilayer TMDCs[76].

A very natural choice for spin injection and for generating proximity exchange in TMDCs are hBN/FM tunnel structures. How large is the proximity-induced exchange in TMDC/hBN/FM heterostructures? What are the optical signatures of such structures? In this manuscript we study tunneling spin injection in TMDC/hBN/FM heterostructures. We calculate the band structure and employ a minimal tight-binding model Hamiltonian to extract orbital, spin-orbit, and proximity exchange parameters for the proximitzed TMDCs, MoS_2, and WS_2. Proximity exchange in the TMDCs is found to be on the order of 1–10 meV, and together with the intrinsic SOC of the TMDC, leads to a valley polarization corresponding to tens of Tesla exchange field for bare TMDCs. Specifically the MoS_2/hBN/Co heterostructure shows a giant valence band spin splitting, of more than 10 meV, due to proximity exchange and hybridization of the TMDC valence band orbitals with Co d orbitals. The corresponding calculated absorption spectrum shows a giant valley splitting of about 8 meV. The valley splitting for WS_2/hBN/Co is of similar magnitude (5 meV), despite the absence of hybridizing d orbitals. In the case of Ni, proximity exchange and valley splittings are reduced (1–3 meV) for both TMDCs. Our investigations should be useful for interpreting spin injection, spin tunneling and optical properties of TMDC/hBN/(Co, Ni) systems. Furthermore, the extracted parameters can be used for transport simulations and further studies of excitonic effects.

II. MODEL HAMILTONIAN

As basis states for our model we use $|\Psi_{\rm CB}\rangle = |d_{z^2}\rangle$ and $|\Psi^\tau_{\rm VB}\rangle = \frac{1}{\sqrt{2}}(|d_{x^2-y^2}\rangle + {\rm i}\tau|d_{xy}\rangle)$, corresponding to conduction band (CB) and valence band (VB) at K ($\tau = 1$) and K' ($\tau = -1$), since the band edges of bare TMDC monolayers are formed by different d-orbitals from the transiton metal[38]. The model Hamiltonian, in the basis which includes electron spin $|\Psi_{\rm CB},\uparrow\rangle$, $|\Psi^\tau_{\rm VB},\uparrow\rangle$, $|\Psi_{\rm CB},\downarrow\rangle$, and $|\Psi^\tau_{\rm VB},\downarrow\rangle$, to describe the band structure of the TMDC close to K and K', in the presence of proximity exchange[55,61] is

$$\mathcal{H} = \mathcal{H}_0 + \mathcal{H}_\Delta + \mathcal{H}_{\rm soc} + \mathcal{H}_{\rm ex} + \mathcal{H}_{\rm R}, \tag{1}$$

$$\mathcal{H}_0 = \hbar v_{\rm F} s_0 \otimes (\tau\sigma_x k_x + \sigma_y k_y), \tag{2}$$

$$\mathcal{H}_\Delta = \frac{\Delta}{2} s_0 \otimes \sigma_z, \tag{3}$$

$$\mathcal{H}_{\rm soc} = \tau s_z \otimes (\lambda_{\rm c}\sigma_+ + \lambda_{\rm v}\sigma_-), \tag{4}$$

$$\mathcal{H}_{\rm ex} = -s_z \otimes (B_{\rm c}\sigma_+ + B_{\rm v}\sigma_-), \tag{5}$$

$$\mathcal{H}_{\rm R} = \lambda_{\rm R}(\tau s_y \otimes \sigma_x - s_x \otimes \sigma_y). \tag{6}$$

Here $v_{\rm F}$ is the Fermi velocity. The Cartesian components k_x and k_y of the electron wave vector are measured from K (K'). The pseudospin Pauli matrices are $\sigma_{\rm i}$ acting on the (CB,VB) subspace and spin Pauli matrices are $s_{\rm i}$ acting on the $(\uparrow,\downarrow)$ subspace, with ${\rm i} = \{0, x, y, z\}$. For shorter notation we introduce $\sigma_\pm = \frac{1}{2}(\sigma_0 \pm \sigma_z)$. TMDCs are semiconductors, and thus $\mathcal{H}_\Delta$ introduces a gap, represented by parameter Δ, in the band structure such that $\mathcal{H}_0 + \mathcal{H}_\Delta$ describes a gapped spectrum with spin-degenerate parabolic CB and VB. In addition the bands are spin-split due to SOC which is captured by the term $\mathcal{H}_{\rm soc}$ with the parameters $\lambda_{\rm c}$ and $\lambda_{\rm v}$ describing the spin splitting of the CB and VB. The Hamiltonian $\mathcal{H}_0 + \mathcal{H}_\Delta + \mathcal{H}_{\rm soc}$ is already suitable to describe the spectrum of intrinsic TMDCs around the band edges at K and K'. In the case when we have a ferromagnetic substrate, proximity exchange effects are present and we introduce the term $\mathcal{H}_{\rm ex}$, with $B_{\rm c}$ and $B_{\rm v}$ describing the proximity induced exchange splittings. Note that this term explicitly breaks time-reversal symmetry and thus the valley degeneracy. Finally, a Rashba term $\mathcal{H}_{\rm R}$, with $\lambda_{\rm R}$ being the Rashba parameter, can be present since a substrate breaks the inversion symmetry of the TMDC.

III. COMPUTATIONAL DETAILS

A. First-principles calculations

The electronic structure calculations and structural relaxation of our geometries are performed with density functional theory (DFT)[91] using Quantum Espresso[92]. Self-consistent calculations are performed with the k-point sampling of $18 \times 18 \times 1$ for the TMDC/hBN/FM heterostrucures. We perform open shell calculations that provide the spin polarized ground

state, when a FM substrate is present. We use an energy cutoff for charge density of 550 Ry, and the kinetic energy cutoff for wavefunctions is 65 Ry for the scalar relativistic pseudopotential with the projector augmented wave method[93] with the Perdew-Burke-Ernzerhof exchange correlation functional[94]. When SOC is included, the fully relativistic versions of the pseudopotentials are used. In addition we include the Hubbard correction for the FMs Co and Ni with $U = 1$ eV[95]. For the relaxation of the heterostructures, we add van der Waals corrections[96,97] and use quasi-newton algorithm based on trust radius procedure. In order to simulate quasi-2D systems, a vacuum of at least 16 Å is used to avoid interactions between periodic images in our slab geometries. Dipole corrections[98] are included for heterostructure calculations to get correct band offsets and internal electric fields. Structural relaxations are performed until all components of all forces were reduced below 10^{-3} [Ry/a_0], where a_0 is the Bohr radius.

B. Absorption spectra calculations for excitons

To compute the excitonic spectra, we employ the effective Bethe-Salpeter equation (BSE)[61,99–103] with the electron-hole interaction mediated by the Rytova-Keldysh potential[104–107] with focus on direct intralayer excitons at zero temperature and without doping effects. The single-particle spectra is given by the model Hamiltonian of Eq.(1) fitted to the first-principles band structures. For the screening lengths of the TMDCs we used the values provided in the study of Berkelbach, Hybertsen, and Reichman[107]. The BSE is solved on a 2D k-grid from -0.5 to 0.5 Å^{-1} in k_x and k_y directions with total discretization of 101×101 points (leading to a spacing of $\Delta k = 10^{-2}$ Å^{-1}). To improve convergence, the Coulomb potential is averaged around each k-point in a square region of $-\Delta k/2$ to $\Delta k/2$ discretized with 101×101 points[61,100].

The absorption spectra incorporating excitonic effects is given by[100,101]

$$\alpha^a(\hbar\omega) = C_0 \sum_N \left| \sum_{cv\vec{k}} A_{cv\vec{k}}(N) p^a_{vc}(\vec{k}) \right|^2 \delta\left(\Omega_N - \hbar\omega\right) \quad (7)$$

with the superindex a indicating the polarization of the light, $C_0 = \left(4\pi^2 e^2\right) / \left(\varepsilon_0 c_l \omega \mathcal{A} \hbar^2\right)$, c_l is the speed of light (the subindex l was added to not be confused with the conduction band index c), $\mathcal{A}$ is the 2D unit area and the dipole matrix element written as $p^a_{nm}(\vec{k}) = \frac{\hbar}{m_0} \left\langle n, \vec{k} \left| \hat{e}_a \cdot \vec{p} \right| m, \vec{k} \right\rangle$. To the final absorption spectra of the intralayer excitons with proximity exchange we apply a lorentzian broadening with energy dependent full width at half-maximum[101,108]

$$\Gamma(\hbar\omega) = \Gamma_1 + \frac{\Gamma_2}{1 + e^{[(E_0 - \hbar\omega)/\Gamma_3]}} \quad (8)$$

using $\Gamma_1 = \Gamma_2 = \Gamma_3 = 10$ meV and E_0 the single-particle energy at K-point for the first allowed optical transition.

IV. TMDC/HBN/FM HETEROSTRUCTURES

A. Geometry

In order to calculate the proximity exchange in a TMDC/hBN/FM heterostructure, we have to find a common unit cell for all compounds minimizing strain effects. In Fig. 1 we show the geometry for MoS_2/hBN/Co, as an exemplary structure. Initial atomic structures are set up with the atomic simulation environment (ASE)[109], as follows. We choose a 4×4 supercell of the TMDC (MoS_2, WS_2), a 5×5 cell of hBN, and a 5×5 cell of the FMs (Co, Ni). For the FM we take three monolayers of hcp Co or fcc(111) Ni. The hBN is placed above the FM, such that the nitrogen sits above the topmost Co/Ni atom, and the boron above the fcc-position above the FM slab, as found by previous studies[19]. The TMDC is placed such above the hBN/FM slab, that a transition metal atom (Mo, W) sits above a nitrogen atom. By choosing the heterostructure as explained, our unit cell contains 173 atoms, with a lattice constant of $a = 12.637$ Å, for all of our considered hybrid geometries. For that we have to modify the lattice constants of the subsystem layers (TMDC, hBN, FM). In Tab. I we give an overview on the original experimental lattice constants, and the new modified lattice constants used for the heterostructures,

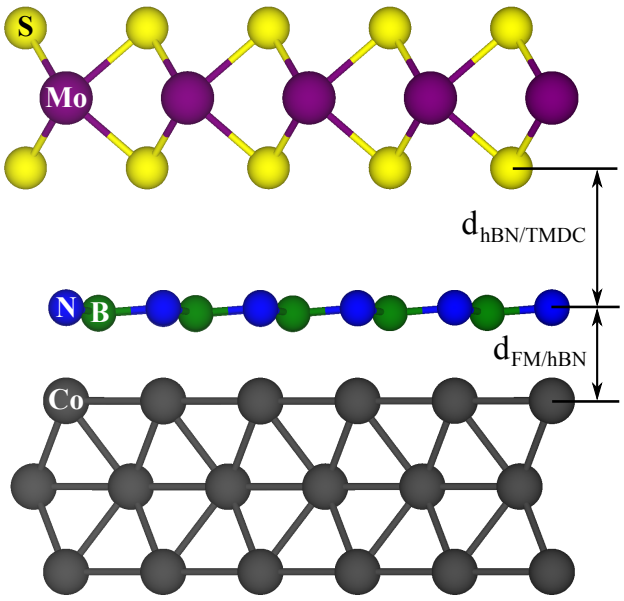

FIG. 1. (Color online) Side view of the TMDC/hBN/FM structure with labels for the atoms and distances. As an example, we show here MoS_2/hBN/Co. The distances between the layers $d_{\text{FM/hBN}}$ and $d_{\text{hBN/TMDC}}$ are listed in Tab. II for all considered heterostructures.

as well as the introduced strain. We can see that a maximum strain of about 1.5% is present for Ni, being still acceptable for our purposes.

	Co	Ni	hBN	MoS_2	WS_2
a (exp.) [Å]	2.507	2.492	2.504	3.150	3.153
a (het.) [Å]	2.527	2.527	2.527	3.159	3.159
strain [%]	0.8	1.4	0.9	0.3	0.2

TABLE I. Overview of the lattice constants and strains for the subsystems used in the TMDC/hBN/FM heterostructures. The experimental a (exp.) lattice constants (Refs. 110–114) of the bulk systems and lattice constants used for the heterostructures a (het.) are given, along with the introduced strain for each subsystem, calculated as $(a_{\mathrm{het}} - a_{\mathrm{exp}})/a_{\mathrm{exp}}$. Note that for nickel, it is the lattice constant of a fcc(111) quasi-hexagonal surface.

To determine the interlayer distances, the atoms of the TMDC, hBN, and the top two Co/Ni layer atoms were allowed to relax only in their z positions (vertical to the layers). The average distances between the layers $d_{\mathrm{FM/hBN}}$ and $d_{\mathrm{hBN/TMDC}}$, as defined in Fig. 1, are listed in Tab. II for all considered geometries. The distances are measured from the average position of the top Co/Ni (bottom S/Se) atoms, with respect to the average position of the N atoms of the hBN layer. The corrugation of the hBN is on average 0.12 Å, independent of the heterostructure. The distances $d_{\mathrm{FM/hBN}}$ between the FMs and hBN are around 2.1 Å, indicating strong bonding. The distances $d_{\mathrm{hBN/TMDC}}$ between the hBN and the TMDCs are roughly 3.15 Å, being in the range of typical van der Waals distances. All these observations are in agreement with previous calculations of hBN on metallic substrates[19,115,116], as well as TMDCs on hBN/metal interfaces[64,65].

B. Band structure and fit results

In Fig. 2 we show the calculated band structures without SOC of all TMDC/hBN/FM heterostructures. Since a lot of bands are involved, originating from the hBN/FM substrate, we only show a projection of the bands originating from the TMDC. In the following we analyze the case of MoS_2/hBN/Co as a representative example. In Fig. 2(a) can see that the band structure closely resembles the bands of pristine MoS_2. The Fermi level is located below the TMDC CB edge. Our calculated band structure is very different compared to other studies of proximity induced exchange[55–57], where the TMDC experiences strong doping, probably due to the polar surfaces of the substrates they consider. Note that a polar surface does not reflect a realistic situation, as surface reconstructions are present in real experiments. This can strongly modify the proximity exchange in experiments, as the hybridization with the substrate is the main origin of proximity exchange. Such effects are absent in a hBN/FM hybrid substrate, due to the hBN buffer layer. Another advantage of our FM/hBN substrate is that the Curie temperature of the standard ferromagnets[111] Co ($T_C = 1388$ K) and Ni ($T_C = 627$ K) is well above room temperature, allowing for experiments at ambient conditions. The ultimate goal is the spin injection into the TMDC via the hBN/FM tunnel junction. If we zoom to the fine structure around the K point, we find that the bands of the TMDC are spin split due to proximity exchange coupling, see Figs. 2(b,c). The splitting of the CB is smaller than that of the VB, both being in the few meV range.

system	MoS_2 hBN Co	MoS_2 hBN Ni	WS_2 hBN Co	WS_2 hBN Ni
Δ [eV]	1.761	1.769	1.910	1.910
v_{F} [$10^5 \frac{\mathrm{m}}{\mathrm{s}}$]	5.303	5.475	6.907	6.908
B_{c} [meV]	1.964	1.697	1.080	1.077
B_{v} [meV]	6.365	2.185	3.629	2.308
dipole [Debye]	1.940	2.871	2.386	3.713
$d_{\mathrm{FM/hBN}}$ [Å]	2.089	2.085	2.089	2.084
$d_{\mathrm{hBN/TMDC}}$ [Å]	3.157	3.217	3.151	3.137

TABLE II. Summary of the fit parameters, calculated dipoles and distances for TMDC/hBN/FM systems without SOC. The Hamiltonian used to fit these systems is $\mathcal{H}_0 + \mathcal{H}_\Delta + \mathcal{H}_{\mathrm{ex}}$, with Δ as the orbital gap of the spectrum, the Fermi velocity v_{F} and B_{c} and B_{v} are the proximity exchange parameters, respectively. The dipole of the structures is given in debye and $d_{\mathrm{hBN/TMDC}}$ is the distance between hBN and the TMDC, and $d_{\mathrm{FM/hBN}}$ is the distance between the FM and hBN, as defined in Fig. 1.

Since SOC effects are turned off, we can fit the band structure around the K point to our model Hamiltonian, neglecting for now $\mathcal{H}_{\mathrm{soc}} + \mathcal{H}_{\mathrm{R}}$. In Fig. 2(b,c), we can see that the bands are nicely reproduced by the model with the fit parameters given in Tab. II. However, we can see that there is a discrepancy between the model and the calculation, especially for the spin-down VB away from the K point. The case of MoS_2/hBN/Co is the only one, where this happens. The origin of this is the hybridization of the VB spin-down state of MoS_2 with Co d-states, as one can see in Fig. 2(a). In Tab. II we summarize our fit parameters for all considered heterostructures. We notice, that especially the parameter B_{v} for the MoS_2/hBN/Co case is very large, which is caused by the previously explained effect of hybridization. In a similar way, an earlier study has shown, that the hybridization with Co d-orbitals can strongly enhance the proximity exchange splitting in graphene on a hBN/Co substrate[19]. Note that also the value of the Hubbard U, which shifts the Co d-levels in energy, affects the 'amount' of hybridization and the spin splitting. Since we have considered $U = 1$ eV only, we can only predict that such

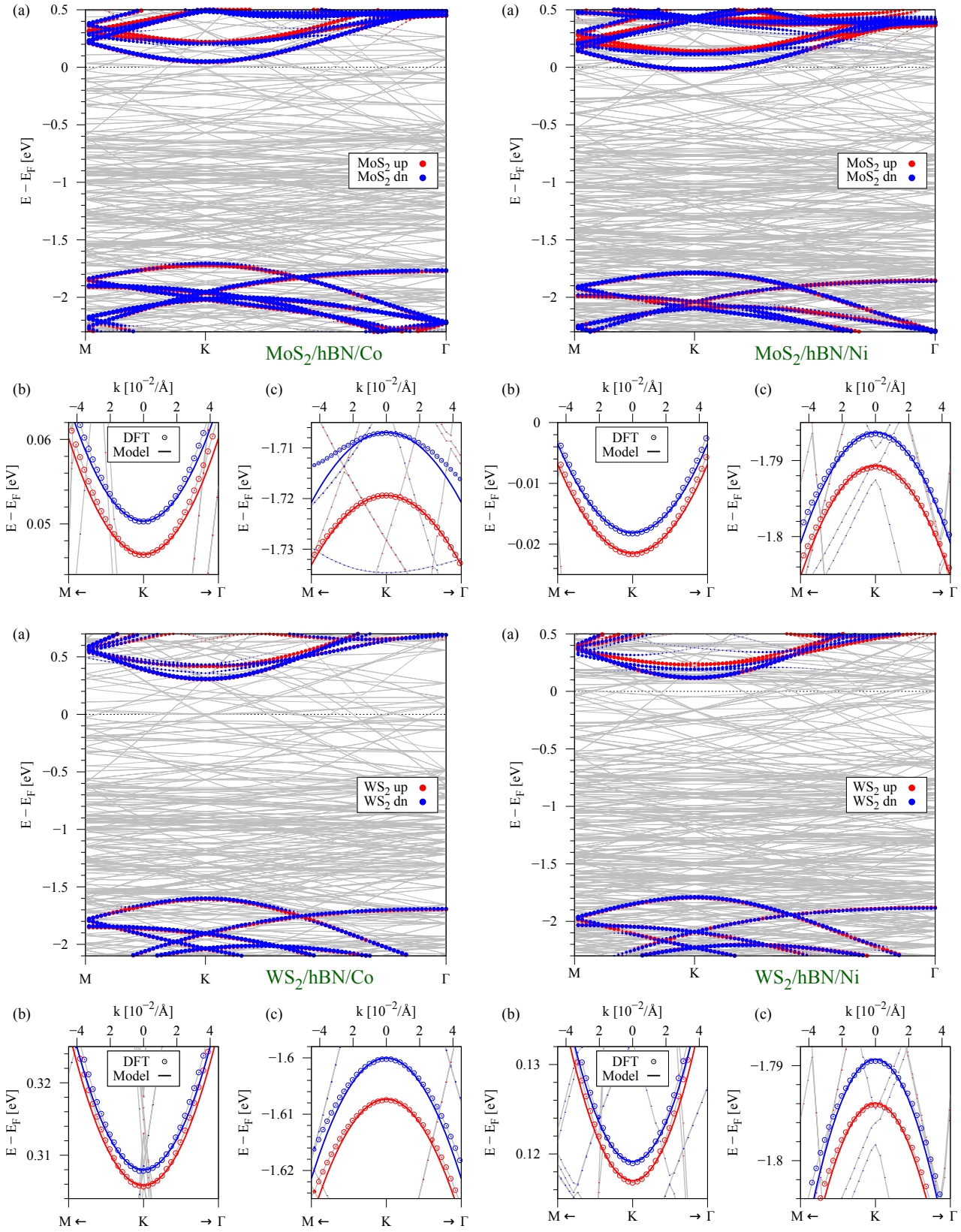

FIG. 2. (Color online) Calculated band structures of TMDC/hBN/FM systems without SOC. (a) Band structure along high symmetry path M-K-Γ. The bands corresponding to the TMDC are highlighted in red (spin up) and blue (spin down). Bands originating from the hBN/FM substrate are plotted in grey. (b) Zoom to the CB edge originating from the TMDC around the K point. Symbols are DFT data and solid lines are the fit to the model Hamiltonian. (c) Same as (b), but for VB edge.

a hybridization is present in experiments, which leads to an enhanced spin splitting.

Unfortunately, we were not able to proper converge the calculations of the TMDC/hBN/FM heterostructures including SOC effects. Therefore, we cannot be completely sure, whether the mentioned hybridization in the MoS_2/hBN/Co structure will remain; the spin-orbit splitting in the TMDC VB is large[38,117] and may shift the corresponding bands to much in energy to spoil the hybridization. However, a similar work of proximity exchange in TMDC/CrI_3 heterostructures has shown, that inclusion of SOC barely affects the proximity exchange parameters[61]. Thus, we believe that proximity exchange on the order of 1–5 meV would still be present when including SOC for our TMDC/hBN/FM structures.

Similar to graphene/hBN/FM stacks[19], we expect that the proximity exchange in the TMDCs also decreases with increasing number of hBN layers between the FM and the TMDC. Unfortunately, due to computational limitations (number of atoms in the supercell), we cannot study more than one hBN layer.

C. TMDC/hBN subsystems

Experimentally it is also interesting to consider the bare MoS_2/hBN and WS_2/hBN heterostructures, without any influence from the FM. For that, we take the TMDC/hBN/FM geometries, but remove the FM layers. After subsequent relaxation, similar as described above,

system	MoS_2 hBN	WS_2 hBN
Δ [eV]	1.756	1.872
v_F [$10^5 \frac{m}{s}$]	5.432	6.786
λ_c [meV]	-1.361	17.03
λ_v [meV]	72.96	208.6
dipole [Debye]	-0.701	-0.703
$d_{hBN/TMDC}$ [Å]	3.330	3.252

TABLE III. Summary of the fit parameters, calculated dipoles and distances for TMDC/hBN systems with SOC. The Hamiltonian used to fit these systems is $\mathcal{H}_0+\mathcal{H}_\Delta+\mathcal{H}_{soc}+\mathcal{H}_R$, with Δ as the orbital gap of the spectrum, the Fermi velocity v_F and λ_c and λ_v are the SOC parameters. The distances are given as defined in Fig. 1.

we calculate the electronic band structures for the *subsystems*, including SOC effects. The corrugation of the hBN reduces to about 20 pm on average, and the distances $d_{hBN/TMDC}$ between hBN and the TMDC are given in Tab. III for the TMDC/hBN stacks. The FM is responsible for the corrugation of the hBN layer, as already pointed out in earlier works[19]. Our model Hamiltonian is also suitable to describe this situation, when neglecting $\mathcal{H}_{ex}$.

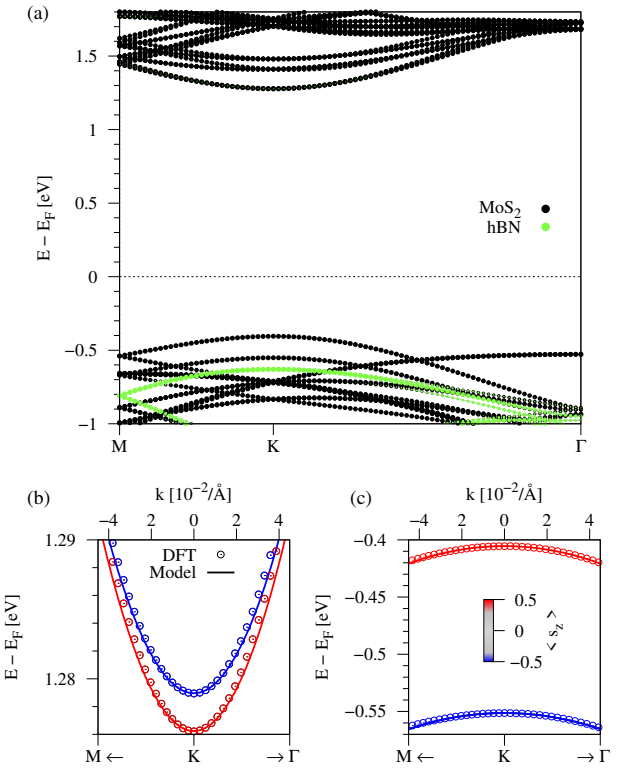

FIG. 3. (Color online) Calculated band structure of MoS_2/hBN including SOC effects. (a) Band structure along high symmetry lines. The bands corresponding to MoS_2 (hBN) are plotted in black (light-green). (b) Zoom to the CB edge. The color corresponds to the s_z-expectation value. Symbols are DFT data and solid lines are fits to the Model Hamiltonian. (c) Same as (b), but for VB edge.

The calculated band structure for MoS_2/hBN is shown in Fig. 3. We find that we can perfectly reproduce the band structure around K and K' valleys, with the fit parameters given in Tab. III. The fit parameters for the TMDC/hBN heterostructures are nearly identical to the ones obtained for the bare TMDC monolayers[38,117]. *We conclude that the hBN has effectively no impact on the TMDC dispersion and SOC.* In principle, one would also expect Rashba SOC due to inversion symmetry breaking, but from previous calculations of graphene/hBN/FM structures[19], we conclude that the proximity induced SOC due to the hBN/FM substrate is negligible, compared to the proximity induced exchange and the giant intrinsic SOC of the bare TMDC[38,117]. Indeed, we find by fitting the model Hamiltonian to the band structure of the TMDC/hBN systems, that $\mathcal{H}_R$ can be neglected, as the s_z spin expectation values of the bands near the K and K' points almost do not differ from ± 0.5, as we can see in Fig. 3.

In conclusion, the extracted proximity exchange (intrinsic SOC) parameters from the calculations of the TMDC/hBN/FM (TMDC/hBN) systems, together with the Hamiltonian, can be used for further studies.

V. PROXIMITY EXCHANGE INDUCED VALLEY SPLITTING

The individually extracted parameters for proximity exchange and SOC, see Tabs. II and III, in combination with our model Hamiltonian can be used to calculate the low energy bands around K and K' point with both effects present. We average the parameters for v_F and Δ from Tabs. II and III, for the MoS_2 and WS_2 based structures. We take the SOC parameters for the two TMDCs from Tab. III, and the proximity exchange parameters from Tab. II. The full parameter sets are summarized in Tab. IV, which we use for the following absorption spectra calculations.

system	MoS_2 hBN Co	MoS_2 hBN Ni	WS_2 hBN Co	WS_2 hBN Ni
Δ [eV]	1.759	1.763	1.891	1.891
v_F [$10^5 \frac{m}{s}$]	5.368	5.454	6.847	6.847
λ_c [meV]	-1.361	-1.361	17.03	17.03
λ_v [meV]	72.96	72.96	208.6	208.6
B_c [meV]	1.964	1.697	1.080	1.077
B_v [meV]	6.365	2.185	3.629	2.308
s. part. [meV]	10.01	1.65	5.10	2.46
exciton [meV]	8.20	0.91	4.76	2.30

TABLE IV. Summary of the model Hamiltonian parameters, combined from Tabs. II and III. The orbital gap parameter Δ, the Fermi velocity v_F, B_c and B_v are the proximity exchange parameters, and λ_c and λ_v are the SOC parameters. The valley splitting calculated from the single particle picture (s. part.) and from the absorption spectra of the first exciton peak.

In this context, one can also generalize the exchange Hamiltonian[55] to $\mathcal{H}_{ex} = -\hat{\mathbf{m}} \cdot \mathbf{s} \otimes (B_c\sigma_+ + B_v\sigma_-)$, with $\hat{\mathbf{m}}$ being a unit vector for the direction of the proximity exchange field and $\mathbf{s}$ is the vector containing Pauli spin matrices. In Fig. 4 we show the calculated model band structure employing the full Hamiltonian with SOC and proximity exchange, setting $\hat{\mathbf{m}} = \hat{m}_z$, for the MoS_2/hBN/Co heterostructure, using the parameters from Tab. IV. Due to the combination of SOC and proximity exchange, time-reversal symmetry is broken and the valley degeneracy is lifted, as can be seen when comparing the spin-split CB at K and K', see Figs. 4(a,c). Remarkably, the order of the spin bands in the CB is the same for the two valleys. For bare TMDCs, the spin splitting in the CB is determined by the corresponding SOC parameter λ_c. For the case of MoS_2, we find that the SOC parameter is comparable in magnitude with the proximity exchange parameter $\lambda_c \approx B_c$, due to the hBN/FM substrate. When the proximity exchange is larger than the SOC, the band ordering of the spin-split CB is the same for both valleys, as can be seen

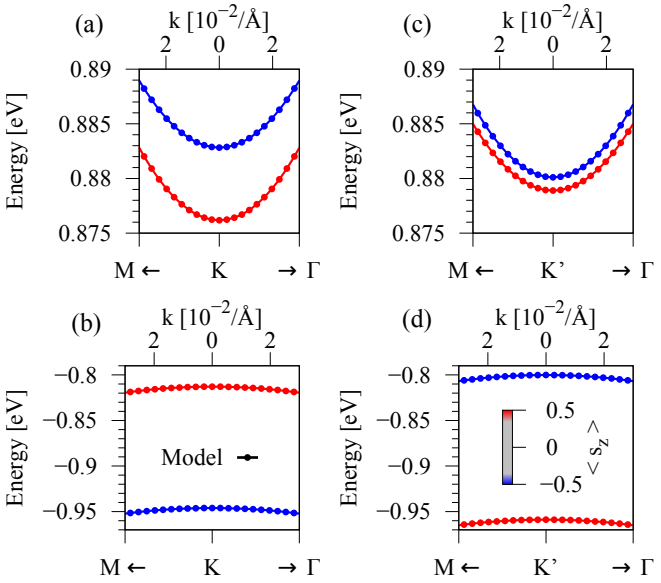

FIG. 4. (Color online) Calculated model band structure employing the full Hamiltonian, for MoS_2/hBN/Co heterostructure using parameters from IV. (a,b) Low energy CB and VB at K point. (c,d) Same as (a,b) but for K' point.

in Figs. 4(a,c). In contrast, the VB SOC parameter is much larger than the corresponding proximity exchange parameter $\lambda_v \gg B_v$, and the VB splitting is dominated by SOC.

For a more realistic assessment of the proximity exchange in the optical spectra, we investigate the valley splitting of the excitonic levels. Employing the parameters summarized in Table IV for the model Hamiltonian and the effective BSE, in Fig. 5 we show the calculated absorption spectra for the TMDC intralayer excitons. For MoS_2 systems, the B excitons are also visible (large peaks around -150 meV) and show a valley splitting with the same value as the A exciton but with opposite sign. The extracted values for the valley splitting of the first exciton peak and within the single particle picture are summarized in Table. IV.

The optical excitation energy difference between K and K' valley for MoS_2/hBN/Co is giant, 8 meV, translating into about 50 T magnetic field for bare TMDCs, if assuming 0.15 meV/T valley splitting[49–52]. A similar giant valley splitting of about 5 meV is achieved in the case of WS_2/hBN/Co, translating to about 30 T magnetic field. Remarkably, in the case of MoS_2/hBN/Co, we have seen that proximity exchange together with band hybridization to *d*-orbitals causes a large VB splitting, leading to the giant valley splitting. In the case of WS_2/hBN/Co, the valley splitting is also giant, but without any band hybridization effects. When Ni is considered as the FM, we find smaller valley splittings, 1 meV (7 T) for MoS_2/hBN/Ni and 2.3 meV (15 T) for WS_2/hBN/Ni, but still the corresponding magnetic fields are quite large, compared to the valley splittings achieved without proximity exchange.

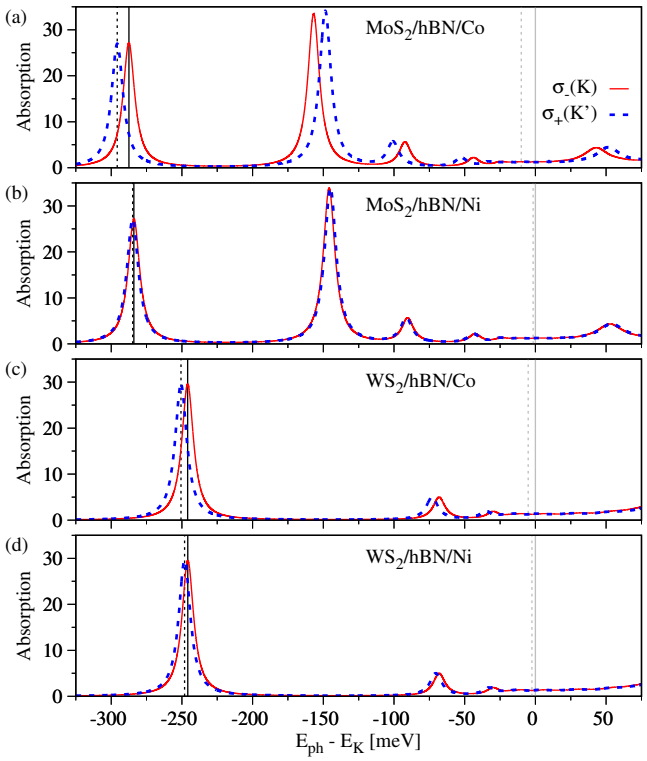

FIG. 5. (Color online) Calculated absorption spectra for (a) MoS_2/hBN/Co, (b) MoS_2/hBN/Ni, (c) WS_2/hBN/Co and (d) WS_2/hBN/Ni. The vertical solid (dashed) lines indicate the energy contribution at K (K') point. Vertical lines close to $E_{\rm ph} - E_{\rm K} = 0$ indicate the single-particle energies while the vertical lines at the first exciton peaks indicate the excitonic contribution. The energy difference between σ_+ and σ_- polarizations is the valley splitting, summarized in Table. IV.

VI. SUMMARY

We have calculated the band structures of TMDC/hBN/FM heterostructures and extracted valuable proximity exchange and SOC parameters, using a minimal low energy Hamiltonian. Due to the hBN buffer layer, the TMDC preserves a great degree of autonomy of its electronic structure. Proximity exchange is found to be on the order of 1–10 meV, depending on the specific FM. Especially in MoS_2/hBN/Co, the spin splitting is giant, about 10 meV, due to proximity exchange and hybridization of Co d states with the spin-down VB of the TMDC. The excitonic absorption spectra, shows a giant splitting of the first exciton peak, translating into a valley polarization corresponding to tens of Tesla exchange field for bare TMDC monolayers. The Ni-based heterostructures show less strong proximity exchange. We believe our calculations provide useful insight to interpret experimental properties of TMDC/hBN/(Co, Ni) devices, for instance related to spin injection, spin tunneling, and optics. Finally, our extracted parameters can be used as input for transport simulations and additional studies of excitonic effects.

ACKNOWLEDGMENTS

This work was supported by DFG SPP 1666, DFG SFB 1277 (project B05 and B07), the European Unions Horizon 2020 research and innovation program under Grant No. 785219, the Alexander von Humboldt Foundation and Capes (grant No. 99999.000420/2016-06).

* klaus.zollner@physik.uni-regensburg.de

[1] I. Žutić, J. Fabian, and S. Das Sarma, Rev. Mod. Phys. **76**, 323 (2004).
[2] W. Han, R. K. Kawakami, M. Gmitra, and J. Fabian, Nat. Nano. **9**, 794 (2014).
[3] J. Fabian, A. Matos-Abiague, C. Ertler, P. Stano, and I. Žutić, Acta Phys. Slov. **57**, 342 (2007).
[4] W. Liu, P. K. J. Wong, and Y. Xu, Prog. Mater. Sci. **99**, 27 (2019).
[5] N. Briggs, S. Subramanian, Z. Lin, X. Li, X. Zhang, K. Zhang, K. Xiao, D. Geohegan, R. Wallace, L.-Q. Chen, M. Terrones, A. Ebrahimi, S. Das, J. Redwing, C. Hinkle, K. Momeni, A. van Duin, V. Crespi, S. Kar, and J. A. Robinson, 2D Mater. **6**, 022001 (2019).
[6] J. H. Zhiquan Yuan and K. Liu, Crystals **7**, 265 (2017).
[7] Z. Hu, Z. Wu, C. Han, J. He, Z. Ni, and W. Chen, Chem. Soc. Rev. **47**, 3100 (2018).
[8] M. V. Kamalakar, A. Dankert, J. Bergsten, T. Ive, and S. P. Dash, Sci. Rep. **4**, 6146 (2014).
[9] W. Fu, P. Makk, R. Maurand, M. Bräuninger, and C. Schönenberger, J. Appl. Phys. **116**, 074306 (2014).
[10] M. Drögeler, C. Franzen, F. Volmer, T. Pohlmann, L. Banszerus, M. Wolter, K. Watanabe, T. Taniguchi, C. Stampfer, and B. Beschoten, Nano Letters **16**, 3533 (2016).
[11] M. Drögeler, F. Volmer, M. Wolter, B. Terrés, K. Watanabe, T. Taniguchi, G. Güntherodt, C. Stampfer, and B. Beschoten, Nano Lett. **14**, 6050 (2014).
[12] M. V. Kamalakar, A. Dankert, P. J. Kelly, and S. P. Dash, Sci. Rep. **6**, 21168 (2016).
[13] M. V. Kamalakar, C. Groenveld, A. Dankert, and S. P. Dash, Nat. Commun. **6**, 6766 (2015).
[14] M. Gurram, S. Omar, and B. J. van Wees, 2D Materials **5**, 032004 (2018).
[15] M. Gurram, S. Omar, and B. J. van Wees, Nat. Commun. **8**, 248 (2017).
[16] L. Banszerus, M. Schmitz, S. Engels, J. Dauber, M. Oellers, F. Haupt, K. Watanabe, T. Taniguchi, B. Beschoten, and C. Stampfer, Sci. Adv. **1**, 1 (2015).
[17] N. Petrone, C. R. Dean, I. Meric, A. M. Van Der Zande, P. Y. Huang, L. Wang, D. Muller, K. L. Shepard, and J. Hone, Nano Lett. **12**, 2751 (2012).
[18] V. E. Calado, S. E. Zhu, S. Goswami, Q. Xu, K. Watanabe, T. Taniguchi, G. C. Janssen, and L. M. Vandersypen, Appl. Phys. Lett. **104** (2014), 10.1063/1.4861627.

[19] K. Zollner, M. Gmitra, T. Frank, and J. Fabian, Phys. Rev. B **94**, 155441 (2016).
[20] M. Gmitra, D. Kochan, P. Högl, and J. Fabian, Phys. Rev. B **93**, 155104 (2016).
[21] M. Gmitra and J. Fabian, Phys. Rev. B **92**, 155403 (2015).
[22] A. W. Cummings, J. H. Garcia, J. Fabian, and S. Roche, Phys. Rev. Lett. **119**, 206601 (2017).
[23] S. Zihlmann, A. W. Cummings, J. H. Garcia, M. Kedves, K. Watanabe, T. Taniguchi, C. Schönenberger, and P. Makk, Phys. Rev. B **97**, 075434 (2018).
[24] S. Omar and B. J. van Wees, Phys. Rev. B **97**, 045414 (2018).
[25] A. Avsar, D. Unuchek, J. Liu, O. L. Sanchez, K. Watanabe, T. Taniguchi, B. Özyilmaz, and A. Kis, ACS Nano **11**, 11678 (2017).
[26] J. C. Leutenantsmeyer, J. Ingla-Aynés, J. Fabian, and B. J. van Wees, Phys. Rev. Lett. **121**, 127702 (2018).
[27] J. Xu, T. Zhu, Y. K. Luo, Y.-M. Lu, and R. K. Kawakami, Phys. Rev. Lett. **121**, 127703 (2018).
[28] Y. K. Luo, J. Xu, T. Zhu, G. Wu, E. J. McCormick, W. Zhan, M. R. Neupane, and R. K. Kawakami, Nano Lett. **17**, 3877 (2017).
[29] L. Li, Y. Yu, G. J. Ye, Q. Ge, X. Ou, H. Wu, D. Feng, X. H. Chen, and Y. Zhang, Nat. Nanotechnol. **9**, 372 (2014).
[30] I. Zutic, J. Fabian, and S. C. Erwin, IBM J. Res. Dev. **50**, 121 (2006).
[31] S. Liang, H. Yang, A. Djeffal, B. Tao, S. Mc-Murtry, S. Mangin, and Y. Lu, J. Appl. Phys. **122**, 164301 (2017).
[32] S. Ahmed and J. Yi, Nano-Micro Lett. **9**, 50 (2017).
[33] M. Kurpas, M. Gmitra, and J. Fabian, Phys. Rev. B **94**, 155423 (2016).
[34] M. Kurpas, M. Gmitra, and J. Fabian, J. Phys. D. Appl. Phys. **51**, 174001 (2018).
[35] A. Avsar, J. Y. Tan, X. Luo, K. H. Khoo, Y. Yeo, K. Watanabe, T. Taniguchi, S. Y. Quek, and B. Özyilmaz, Nano Lett. **17**, 5361 (2017).
[36] J. Qiao, X. Kong, Z. X. Hu, F. Yang, and W. Ji, Nat. Commun. **5**, 1 (2014).
[37] H. Liu, A. T. Neal, Z. Zhu, Z. Luo, X. Xu, D. Tománek, and P. D. Ye, ACS Nano **8**, 4033 (2014).
[38] A. Kormányos, G. Burkard, M. Gmitra, J. Fabian, V. Zólyomi, N. D. Drummond, V. Fal'ko, and V. Fal'ko, 2D Materials **2**, 022001 (2014), 1410.6666.
[39] G.-B. Liu, D. Xiao, Y. Yao, X. Xu, and W. Yao, Chem. Soc. Rev. **44**, 2643 (2015).
[40] P. Tonndorf, R. Schmidt, P. Böttger, X. Zhang, J. Börner, A. Liebig, M. Albrecht, C. Kloc, O. Gordan, D. R. T. Zahn, S. Michaelis de Vasconcellos, and R. Bratschitsch, Opt. Express **21**, 4908 (2013).
[41] S. Tongay, J. Zhou, C. Ataca, K. Lo, T. S. Matthews, J. Li, J. C. Grossman, and J. Wu, Nano Lett. **12**, 5576 (2012).
[42] G. Eda, H. Yamaguchi, D. Voiry, T. Fujita, M. Chen, and M. Chhowalla, Nano Lett. **11**, 5111 (2011).
[43] D. Xiao, G.-B. Liu, W. Feng, X. Xu, and W. Yao, Phys. Rev. Lett. **108**, 196802 (2012).
[44] S. A. Vitale, D. Nezich, J. O. Varghese, P. Kim, N. Gedik, P. Jarillo-Herrero, D. Xiao, and M. Rothschild, Small **14**, 1801483 (2018).
[45] F. Langer, C. P. Schmid, S. Schlauderer, M. Gmitra, J. Fabian, P. Nagler, C. Schüller, T. Korn, P. G. Hawkins, J. T. Steiner, U. Huttner, S. W. Koch, M. Kira, and R. Huber, Nature **557**, 76 (2018).
[46] J. R. Schaibley, H. Yu, G. Clark, P. Rivera, J. S. Ross, K. L. Seyler, W. Yao, and X. Xu, Nature Reviews Materials **1**, 16055 (2016).
[47] Y. Ye, J. Xiao, H. Wang, Z. Ye, H. Zhu, M. Zhao, Y. Wang, J. Zhao, X. Yin, and X. Zhang, Nat. Nanotechnol. **11**, 598 (2016).
[48] D. Zhong, K. L. Seyler, X. Linpeng, R. Cheng, N. Sivadas, B. Huang, E. Schmidgall, T. Taniguchi, K. Watanabe, M. A. McGuire, W. Yao, D. Xiao, K.-M. C. Fu, and X. Xu, Science Advances **3**, e1603113 (2017).
[49] A. Srivastava, M. Sidler, A. V. Allain, D. S. Lembke, A. Kis, and A. Imamolu, Nature Physics **11**, 141 (2015).
[50] G. Aivazian, Z. Gong, A. M. Jones, R. L. Chu, J. Yan, D. G. Mandrus, C. Zhang, D. Cobden, W. Yao, and X. Xu, Nature Physics **11**, 148 (2015).
[51] Y. Li, J. Ludwig, T. Low, A. Chernikov, X. Cui, G. Arefe, Y. D. Kim, A. M. van der Zande, A. Rigosi, H. M. Hill, S. H. Kim, J. Hone, Z. Li, D. Smirnov, and T. F. Heinz, Phys. Rev. Lett. **113**, 266804 (2014).
[52] D. MacNeill, C. Heikes, K. F. Mak, Z. Anderson, A. Kormányos, V. Zólyomi, J. Park, and D. C. Ralph, Phys. Rev. Lett. **114**, 037401 (2015).
[53] Y. Ji, Y. Song, J. Zou, and W. Mi, Physical Chemistry Chemical Physics **20**, 6100 (2018).
[54] N. Li, J. Zhang, Y. Xue, T. Zhou, and Z. Yang, Physical Chemistry Chemical Physics **20**, 3805 (2018).
[55] J. Qi, X. Li, Q. Niu, and J. Feng, Physical Review B **92**, 121403 (2015).
[56] Q. Zhang, S. A. Yang, W. Mi, Y. Cheng, and U. Schwingenschlögl, Advanced Materials **28**, 959 (2016).
[57] L. Xu, M. Yang, L. Shen, J. Zhou, T. Zhu, and Y. P. Feng, Phys. Rev. B **97**, 041405 (2018).
[58] C. Zhao, T. Norden, P. Zhang, P. Zhao, Y. Cheng, F. Sun, J. P. Parry, P. Taheri, J. Wang, Y. Yang, T. Scrace, K. Kang, S. Yang, G. X. Miao, R. Sabirianov, G. Kioseoglou, W. Huang, A. Petrou, and H. Zeng, Nature Nanotechnology **12**, 757 (2017).
[59] K. Seyler, D. Zhong, B. Huang, X. Linpeng, N. P. Wilson, T. Taniguchi, K. Watanabe, W. Yao, D. Xiao, M. A. McGuire, K. M. Fu, and X. Xu, Nano Letters (2018), 10.1021/acs.nanolett.8b01105.
[60] B. Peng, Q. Li, X. Liang, P. Song, J. Li, K. He, D. Fu, Y. Li, C. Shen, H. Wang, C. Wang, T. Liu, L. Zhang, H. Lu, X. Wang, J. Zhao, J. Xie, M. Wu, L. Bi, L. Deng, and K. P. Loh, ACS Nano **11**, 12257 (2017).
[61] K. Zollner, P. E. Faria Junior, and J. Fabian, Phys. Rev. B **100**, 085128 (2019).
[62] D. Somvanshi, S. Kallatt, C. Venkatesh, S. Nair, G. Gupta, J. K. Anthony, D. Karmakar, and K. Majumdar, Phys. Rev. B **96**, 205423 (2017).
[63] O. L. Sanchez, D. Ovchinnikov, S. Misra, A. Allain, and A. Kis, Nano Lett. **16**, 5792 (2016).
[64] M. Farmanbar and G. Brocks, Phys. Rev. B **93**, 085304 (2016).
[65] M. Farmanbar and G. Brocks, Phys. Rev. B **91**, 161304 (2015).
[66] X. Cui, E.-M. Shih, L. A. Jauregui, S. H. Chae, Y. D. Kim, B. Li, D. Seo, K. Pistunova, J. Yin, J.-H. Park, H.-J. Choi, Y. H. Lee, K. Watanabe, T. Taniguchi, P. Kim, C. R. Dean, and J. C. Hone, Nano Lett. **17**, 4781 (2017).
[67] Y. Zhao, K. Xu, F. Pan, C. Zhou, F. Zhou, and Y. Chai, Adv. Funct. Mater. **27**, 1603484 (2017).
[68] T. Garandel, R. Arras, X. Marie, P. Renucci, and L. Calmels, Phys. Rev. B **95**, 075402 (2017).

[69] A. Rai, H. Movva, A. Roy, D. Taneja, S. Chowdhury, and S. Banerjee, Crystals **8**, 316 (2018).
[70] D. S. Schulman, A. J. Arnold, and S. Das, Chem. Soc. Rev. **47**, 3037 (2018).
[71] Y. Guo, Y. Han, J. Li, A. Xiang, X. Wei, S. Gao, and Q. Chen, ACS Nano **8**, 7771 (2014).
[72] M. Zhu, W. Luo, N. Wu, X.-a. Zhang, and S. Qin, Appl. Phys. Lett. **112**, 183102 (2018).
[73] J. Su, L.-p. Feng, X. Zheng, C. Hu, H. Lu, and Z. Liu, ACS Appl. Mater. Interfaces **9**, 40940 (2017).
[74] J. Wang, Q. Yao, C.-W. Huang, X. Zou, L. Liao, S. Chen, Z. Fan, K. Zhang, W. Wu, X. Xiao, C. Jiang, and W.-W. Wu, Adv. Mater. **28**, 8302 (2016).
[75] N. Kaushik, D. Karmakar, A. Nipane, S. Karande, and S. Lodha, ACS Appl. Mater. Interfaces **8**, 256 (2016).
[76] S. Liang, H. Yang, P. Renucci, B. Tao, P. Laczkowski, S. Mc-Murtry, G. Wang, X. Marie, J.-M. George, S. Petit-Watelot, A. Djeffal, S. Mangin, H. Jaffrès, and Y. Lu, Nat. Commun. **8**, 14947 (2017).
[77] W. Wang, Y. Liu, L. Tang, Y. Jin, T. Zhao, and F. Xiu, Sci. Rep. **4**, 1 (2014).
[78] A. Dankert, L. Langouche, M. V. Kamalakar, and S. P. Dash, ACS Nano **8**, 476 (2014).
[79] N. Hayakawa, I. Muneta, T. Ohashi, K. Matsuura, J. Shimizu, K. Kakushima, K. Tsutsui, and H. Wakabayashi, Jpn. J. Appl. Phys. **57**, 04FP13 (2018).
[80] H. M. W. Khalil, M. F. Khan, J. Eom, and H. Noh, ACS Appl. Mater. Interfaces **7**, 23589 (2015).
[81] Y. Liu, H. Wu, H.-C. Cheng, S. Yang, E. Zhu, Q. He, M. Ding, D. Li, J. Guo, N. O. Weiss, Y. Huang, and X. Duan, Nano Lett. **15**, 3030 (2015).
[82] Y. Song and H. Dery, Phys. Rev. Lett. **111**, 026601 (2013).
[83] K. Tian, Z. Yue, D. Magginetti, M. E. Raikh, and A. Tiwari, Phys. Rev. B **95**, 174428 (2017).
[84] J. R. Durán Retamal, D. Periyanagounder, J.-J. Ke, M.-L. Tsai, and J.-H. He, Chem. Sci. **9**, 7727 (2018).
[85] H. Schmidt, F. Giustiniano, and G. Eda, Chem. Soc. Rev. **44**, 7715 (2015).
[86] S. L. Li, K. Wakabayashi, Y. Xu, S. Nakaharai, K. Komatsu, W. W. Li, Y. F. Lin, A. Aparecido-Ferreira, and K. Tsukagoshi, Nano Lett. **13**, 3546 (2013).
[87] H. Ochoa and R. Roldán, Phys. Rev. B **87**, 245421 (2013).
[88] T. Habe and M. Koshino, Phys. Rev. B **93**, 075415 (2016).
[89] F. Yang, L. Wang, and M. W. Wu, Phys. Rev. B **92**, 155414 (2015).
[90] F. Yang and M. W. Wu, Phys. Rev. B **93**, 235433 (2016).
[91] P. Hohenberg and W. Kohn, Phys. Rev. **136**, B864 (1964).
[92] P. Giannozzi, S. Baroni, N. Bonini, M. Calandra, R. Car, C. Cavazzoni, D. Ceresoli, G. L. Chiarotti, M. Cococcioni, I. Dabo, A. D. Corso, S. Fabris, G. Fratesi, S. de Gironcoli, R. Gebauer, U. Gerstmann, C. Gougoussis, A. Kokalj, M. Lazzeri, L. Martin-Samos, N. Marzari, F. Mauri, R. Mazzarello, S. Paolini, A. Pasquarello, L. Paulatto, C. Sbraccia, S. Scandolo, G. Sclauzero, A. P. Seitsonen, A. Smogunov, P. Umari, and R. M. Wentzcovitch, J. Phys.: Condens. Mat. **21**, 395502 (2009).
[93] G. Kresse and D. Joubert, Phys. Rev. B **59**, 1758 (1999).
[94] J. P. Perdew, K. Burke, and M. Ernzerhof, Phys. Rev. Lett. **77**, 3865 (1996).
[95] A. I. Liechtenstein, V. I. Anisimov, and J. Zaanen, Phys. Rev. B **52**, R5467 (1995).
[96] S. Grimme, J. Comput. Chem. **27**, 1787 (2006).
[97] V. Barone, M. Casarin, D. Forrer, M. Pavone, M. Sambi, and A. Vittadini, J. Comput. Chem. **30**, 934 (2009).
[98] L. Bengtsson, Phys. Rev. B **59**, 12301 (1999).
[99] M. Rohlfing and S. G. Louie, Phys. Rev. B **62**, 4927 (2000).
[100] B. Scharf, G. Xu, A. Matos-Abiague, and I. Žutić, Phys. Rev. Lett. **119**, 127403 (2017).
[101] B. Scharf, D. Van Tuan, I. Žutić, and H. Dery, Journal of Physics: Condensed Matter **31**, 203001 (2019).
[102] D. Tedeschi, M. De Luca, P. E. Faria Junior, A. Granados del Águila, Q. Gao, H. H. Tan, B. Scharf, P. C. M. Christianen, C. Jagadish, J. Fabian, and A. Polimeni, Phys. Rev. B **99**, 161204 (2019).
[103] P. E. Faria Junior, M. Kurpas, M. Gmitra, and J. Fabian, Phys. Rev. B **100**, 115203 (2019).
[104] N. S. Rytova, Moscow University Physics Bulletin **3**, 18 (1967).
[105] L. Keldysh, Soviet Journal of Experimental and Theoretical Physics Letters **29**, 658 (1979).
[106] P. Cudazzo, I. V. Tokatly, and A. Rubio, Phys. Rev. B **84**, 085406 (2011).
[107] T. C. Berkelbach, M. S. Hybertsen, and D. R. Reichman, Phys. Rev. B **88**, 045318 (2013).
[108] H. Haug and S. W. Koch, *Quantum Theory of the Optical and Electronic Properties of Semiconductors: Fifth Edition* (World Scientific Publishing Company, 2009).
[109] S. R. Bahn and K. W. Jacobsen, Comput. Sci. Eng. **4**, 56 (2002).
[110] C. M. Singal and T. P. Das, Phys. Rev. B **16**, 5068 (1977).
[111] C. Kittel, *Introduction to Solid State Physics* (Wiley, 2004).
[112] A. Catellani, M. Posternak, A. Baldereschi, and A. J. Freeman, Phys. Rev. B **36**, 6105 (1987).
[113] N. Wakabayashi, H. G. Smith, and R. M. Nicklow, Physical Review B **12**, 659 (1975).
[114] W. J. Schutte, J. L. De Boer, and F. Jellinek, Journal of Solid State Chemistry **70**, 207 (1987).
[115] M. Bokdam, G. Brocks, M. I. Katsnelson, and P. J. Kelly, Physical Review B **90**, 085415 (2014).
[116] P. Lazić, G. M. Sipahi, R. K. Kawakami, and I. Žutić, Phys. Rev. B **90**, 085429 (2014).
[117] K. Zollner, P. E. F. Junior, and J. Fabian, (2019), arXiv:1909.10763.